Thermo- and pH-Responsive Fibrillization of Squid Suckerin A1H1 Peptide

Journal:	*Nanoscale*
Manuscript ID	NR-ART-10-2019-009271.R1
Article Type:	Paper
Date Submitted by the Author:	15-Jan-2020
Complete List of Authors:	Sun, Yunxiang; Clemson University, Physics and Astronomy Ding, Feng; Clemson University, Physics and Astronomy

SCHOLARONE™
Manuscripts

Thermo- and pH-Responsive Fibrillization of Squid Suckerin A1H1 Peptide

Yunxiang Sun[1,2,*], and Feng Ding[2,*]

[1] Department of Physics, Ningbo University, Ningbo 315211, China

[2] Department of Physics and Astronomy, Clemson University, Clemson, SC 29634, United States

Abstract

Stimuli-responsive smart materials have attracted great attention with numerous applications in nanotechnology, sensing, and biomedicine. Suckerin family proteins found in squid ring teeth represent such a class of peptide-based smart materials with their self-assemblies featuring excellent thermo-plasticity and pH-dependence. Similar to block copolymers, suckerin proteins are comprised of two repeating sequence motifs, where M1 motifs are abundant of alanine and histidine residues and M2 rich in glycine. Experimental studies of suckerin assemblies suggested that M1 regions mainly formed nano-confined β-sheets within an amorphous matrix made of M2 modules stabilizing these β-rich nano-assemblies. The histidine-containing M1 modules are believed to govern the pH- and temperature-sensitive properties of suckerin assemblies. To better understand the stimuli-responsive properties of suckerin assemblies at the molecular level, we systematically studied the self-assembly dynamics of A1H1 peptides – a representative M1 sequence – at different temperatures and pH conditions with atomistic discrete molecular dynamics simulations. Our simulations with twenty A1H1 peptides demonstrated that below a transition temperature T_{agg} they could readily self-assemble from isolated monomers into well-defined β-sheet nanostructures by both primary and secondary nucleation of β-sheets and subsequent aggregation growth via elongation and coagulation. Interestingly, the dissociation of pre-formed A1H1 β-sheet nanostructures featured a melting temperature T_m higher than T_{agg}, exhibiting the thermal hysteresis characteristic to first-order phase transitions with high energy barriers. In acidic environments where all histidine residues were protonated, the stability of A1H1 β-sheet nano-assemblies was reduced and the β-rich assemblies easily dissociated into unstructured monomers at significantly lower temperatures than in the neutral solution. The computationally-derived molecular mechanisms to the pH- and temperature-dependent A1H1 self-assembly will help understand the supramolecular assembly structures and functions of the large suckerin family and aid in the future design of peptide-based stimuli-responsive smart materials.

Introduction

The stimuli-responsive smart materials based on the synthesis of block copolymers have found numerous applications in drug delivery, diagnostics, tissue engineering, biosensors and smart optical systems[1-3]. The self-assembly of block copolymer-like proteins (*e.g.*, suckerin[4], spider silk[5] and marine snail[6]) represent a novel class of peptide-based smart polymers with stimuli-responsive properties. Indeed, the peptide-based self-assembly into supramolecular nanostructures has attracted great attention due to its important role in biology associated with many functional or disease-related amyloids and also a range of potential applications in energy, food science, biomedicine, and bio-nanotechnology[7-9]. The self-assembly process is spontaneous and driven by non-covalent interactions including van der Waals, electrostatic, hydrogen-bonding, π–π stacking and hydrophobic packing[10, 11]. Numerous experimental studies demonstrated that short peptides with specific sequences could self-assemble into well-defined nano-architectures such as nanotubes, nanovesicles, and nano-tapes depending on experimental conditions[12-16]. The high biocompatibility with biological origin, control of structures, low immunogenicity, and versatile functionality of self-assembled peptide nanostructures empower their broad applications in biomedicine and bio-nanotechnology (*e.g.,* drug delivery, bioimaging, and biosensors)[7].

Functional assembly of proteins and peptides widely exists in nature, including human (e.g. blood fibrin[17], and actin fibrils[18]), animal (squid sucker ring teeth[19] and spider silk[5]), bacteria (curli[20] and Fap[21] fibrils) and food (β-lactoglobulin[22, 23] and lysozyme[24]). Different from disease-related amyloid peptides such as amyloid-β in Alzheimer's disease[25, 26] and amylin in type-2 diabetes[26-28] where their aberrant aggregation could induce numerous degenerative diseases[26, 29, 30], the functional amyloid peptides in the form of stable β-sheet nanostructures are naturally abundant in organisms ranging from bacteria to human with various functional roles[19,31, 32]. Among these functional amyloid peptides, the suckerin proteins (discovered in the sucker ring teeth of squids, SRT) were widely studied experimentally due to their robust mechanical properties, highly modular peptide building blocks and potential applications in drug delivery[33-38]. For example, Ding *et al.*[36] found that the suckerin-39 (now identified as suckerin-19[19]) could aggregate into β-sheet rich soluble oligomers at a concentration of ~1 mg/ml in water with a similar secondary structure to its native structure, but not in acidic environment. At a higher concentration of ~6 mg/ml the suckerin-39 protein formed soluble oligomers in both water and acidic environment with the β-sheet structure content higher in neutral than in acidic solvents[36]. Since the β-sheet content in the suckerin assembles could be regulated by changing solvent conditions (*e.g.* pH, urea concentration, temperature), their potential applications in drug delivery and release were also well studied[33, 38]. Especially, the pH-dependent β-sheet content in suckerin-based nanostructures allowed the encapsulation of the drug molecules and then release at a low pH environment, making them a promising nanomedicine candidate for controlled drug release[33, 38]. In addition, suckerin assemblies also exhibit thermoplastic property, where they could be melted and reshaped multiple times without the loss of their mechanical characteristics[4, 37, 39, 40] and the β-sheet content was also found to be temperature-dependent[39, 40]. This thermoplastic property of suckerin assembly allows their promising potential applications in 3D printing and tissue regeneration.

Although properties and potential applications of protein assemblies formed by suckerin family proteins were well demonstrated by numerous experimental studies[4, 33-35, 37-40], the atomic details of the self-assembly process and molecular insights to the thermo- and pH-dependence of the assemblies are still exclusive due to their large sizes and intrinsic heterogeneity of the assembly process. Molecular insights bridging these knowledge gaps will be helpful for enabling future applications of suckerin assemblies and the design of peptide-based stimuli-responsive smart materials. There are about 38 suckerin family proteins with the sequence length ranging from 73 to 597[19]. Almost all suckerin proteins exhibit the block copolymer-like modular structures with repeating sequence motifs of [Pro-M1-Pro-M2][19, 36], where M1 and M2 are distinct sequence motifs flanked by Proline residues. The M1 module is typically 10-15 residues abundant of alanine (A) and histidine (H) while including a few serine (S), threonine (T) and valine (V) residues[4, 19, 36]. The M2 module is glycine (G) rich and decorated by scattered tyrosine (Y) and leucine (L) residues with the length varying from 20 to 40 residues[19, 36]. Wide angle X-ray scattering (WAXS) and solution NMR studies showed that the M1 modules mainly adopted nano-confined β-sheets within an amorphous matrix made of M2 modules[19, 37, 41, 42]. Since histidine residues in M1 modules can be protonated at low pH, they are believed to contribute to the pH-dependence of A1H1 assembly. As a result, the representative A1H1 (AATAVSHTTHHA) peptide of M1 modules that are highly abundant in suckerin family proteins has been well studied experimentally[35, 42, 43]. The A1H1 sequence is amphiphilic where the hydrophobic head A1 (AATAVS) region is postulated to drive A1H1 self-aggregation into β-sheets and the hydrophilic tail H1 (HTTHHA) region maintain the high solubility[35, 43]. Experimental studies demonstrated that A1H1 could assemble into β-sheet rich aggregates in water and chiral nanostructures in the presence of polar solvent, acetonitrile[35, 42]. Owing to the short sequence, pH-dependence and the ability to form β-sheet aggregates as in the full-length suckerin proteins, A1H1 fragment represents an ideal model system to computationally investigate the self-assembly process and the stimuli-responses of suckerin assemblies at the molecular level.

Here, we applied all-atom discrete molecular dynamics (DMD), a rapid and predictive molecular dynamics algorithm for studying protein folding and aggregation[44-46], to systematically study the self-assembly as well as dissociation dynamics of A1H1 peptides at different temperatures in neutral and acidic environments. Our simulation results with twenty A1H1 peptides demonstrated that A1H1 could aggregate into cross-β fibril-like nanostructures below an aggregation transition temperature T_{agg} in the neutral solution. The dissociation of pre-formed A1H1 β-sheet nanostructures featured a melting temperature T_m that was significantly higher than T_{agg} under the same solution condition – i.e., displaying a thermal hysteresis characteristic to first-order phase transitions with high energy barriers. In the acidic environment where all histidine residues were protonated, the stability of β-sheet nanostructures was significantly reduced by electrostatic repulsions. The ordered nano-assemblies at temperatures lower than T_{agg} were easily disrupted into isolated monomers adopting coil conformations. By recapitulating the experimentally observed pH- and temperature-responses of A1H1 assemblies, our computational results not only offered molecular insights for better understanding the supramolecular assembly structures and functions of the large suckerin family, but also provided a predictive computational tool for

the future design of smart stimuli-responsive materials using peptides.

Results and Discussion

A1H1 peptides self-assembled into β-rich nanostructures below a critical aggregation temperature. To investigate the structures and dynamics of A1H1 self-assembly, we systematically simulated twenty A1H1 peptides starting from isolated unstructured monomers at different temperatures ranging from 0.50 to 0.60 in reduced DMD temperature unit[47] under the neutral solution environment (Methods). At each temperature, twenty independent simulations each of which started with different initial coordinates and velocities and lasted 350 ns were performed. A cubic simulation box with the periodic boundary condition and the dimension of ~13.1 nm was used and the corresponding peptide concentration was ~14.8 mM. To avoid the potential bias originated from the initial configurations, only the last 100 ns simulation data from each independent simulation was used in the analysis of averaged structural properties.

A1H1 displayed a temperature-dependent propensity to adopt β-sheet structures (Fig. 1a). At low temperatures from 0.50 to 0.52, the β-sheet content of A1H1 aggregates was over 70.0%, in agreement with previous experimental values (~72.9%) determined by FTIR[35, 42]. As the temperature increased above 0.56, no stable β-sheet structure was observed. The mid-point temperature for ~35% β-sheet content was around 0.55. We also analyzed the average number of backbone hydrogen bonds in β-sheet and non-β-sheet structures at different temperatures (Fig. 1b). Consistent with the formation of ordered secondary structures, the majority of backbone hydrogen bonds was formed in β-sheets, indicating that β-sheet structures were the dominated secondary structures in A1H1 self-assemblies. Similarly, as the temperature increased up to 0.55, the number of hydrogen bonds was also significantly decreased. The nearly 1:1 ratio of hydrogen bonds in anti-parallel or parallel alignment of β-strands[48] indicated that A1H1 could form both anti-parallel and parallel β-sheets (Fig. 1c).

We also computed the size distribution of aggregates during the last 100 ns simulations (Fig. 1d). The aggregate size corresponded to the total number of peptides in a peptide cluster which were connected by inter-molecular heavy atom contacts[46, 48]. At low temperatures of 0.50-0.52, A1H1 displayed a strong self-association propensity with almost all peptides assembled into a single aggregate – *i.e.*, the oligomer size equal to the total number of peptides in simulations. As the temperature increased from 0.54 to 0.55, the most populated aggregate size decreased from 15-20 to 1-3. At temperatures higher than 0.56, the peptides mostly stayed as isolated monomers. We further calculated the size probability distribution of β-sheet oligomers, where two β-sheets belonged to the same β-sheet oligomer if they were connected by at least one inter-molecular heavy atom pair[48, 49] (Fig. 1e). The β-sheet oligomer size was referred as the total number of peptides adopting β-strand conformations in a β-sheet oligomer. The most dominated β-sheet oligomer size at low temperatures 0.50-0.52 was equal to the total number of simulated peptides, demonstrating that all peptides self-assembled into one single β-sheet oligomer. The calculation of the mass-weighted average β-sheet size (i.e., the number of strands in a multi-strand β-sheet)[50-52] suggested that A1H1 peptides mainly adopted 10-strand β-sheets (Fig. 1f), although low probabilities of 6- and 20-strand β-sheets

were also observed. Together with the size distribution of β-sheet oligomers (Fig. 1e), our results indicated that twenty A1H1 peptides could self-assemble into one-, two- and three-layered β-sheet oligomers at low temperatures (Fig. 1h-j), but with the two-layered β-sheet aggregates as the dominant species as estimated by dividing the average β-sheet oligomer size of ~20 with the mass-weighted averaged β-sheet size of ~10[50].

To characterize interactions stabilizing the β-rich assembly structures, we computed the residue-wise inter-peptide contact frequency maps between either the backbone or the sidechain atoms of different residues in A1H1 aggregates obtained at low temperatures of 0.50-0.52 (Fig. 1g). The backbone contact frequency map to the left were consent with the formation of both parallel and anti-parallel in-registered β-sheets (Fig. 1c, 1h-j). In the sidechain-sidechain contact frequency map (the right panel of Fig. 1g), the high contact probabilities along the diagonal (e.g., the high inter-peptide contact frequencies of valine5-valine5, and histidine7-histindine7) indicated that the sidechains of hydrophobic N- or hydrophilic C-termini tended to interact among themselves respectively, driven by hydrophobic interactions and π-π stacking between the neutrally-charged histidines. Overall, our simulation results showed that A1H1 peptides had strong propensities to self-assemble into β-sheet nanostructures below a critical temperature T_{agg} ~ 0.55, above which the peptides stayed as isolated monomers in coil conformations. We note that T_{agg} = 0.55 kcal/(mol·k$_B$) in our DMD simulations corresponds to ~275 K (Methods). Such a low aggregation temperature is consistent with experimental studies[35], where the formation of β-sheet rich aggregates by ~4 mM A1H1 in water was only observed after one-week incubation at the room temperature. Only in the presence of acetonitrile, the peptides started to form fibrils readily. Since the free energy barrier for aggregation was predominantly the entropy loss upon forming the aggregation nucleus, lower temperatures with smaller free energy barriers were required to observe aggregation during the course of DMD simulations.

The self-assembly dynamics of A1H1 peptides and the aggregation free energy landscape. Ensemble conformational analysis suggested that A1H1 could self-assemble into predominantly two-layered β-sheets, although single- and three-layered β-sheet nanostructures were also observed. We further examined individual trajectories for the self-assembling dynamics of forming ordered single-, two- and three-layered β-sheet aggregates (Fig. 2a-c, respectively) by monitoring the time evolution of the sizes of the largest oligomer, the largest β-sheet oligomer, the largest β-sheet, and the mass-weighted average β-sheet size[46, 48-50]. A1H1 first assembled into mostly unstructured small oligomers that were dynamic in sizes (e.g., ~5 ns in Fig. 2a, ~5 ns in Fig. 2b, and ~4 ns in Fig. 2c), within which single- (e.g., ~16 ns in Fig. 2a, ~18 ns in Fig. 2b, and ~25 ns in Fig. 2c) or two-layered (e.g, ~25 ns in Fig. 2c) β-sheets started to nucleate, known as the primary nucleation process[53-55]. These β-sheet aggregates could grow as other unstructured peptides docked onto the elongation ends of the pre-formed β-sheet oligomers and subsequently converted into β-strands (*e.g.,* ~50 ns in Fig. 2a, ~18 ns in Fig. 2b, and ~30 ns in Fig. 2c). Such an elongation process of pre-formed β-sheet aggregates is known as the dock-lock mechanism for fibril growth based on extensive molecular dynamics simulations of amyloid peptides[60]. The side-chain surfaces of these initially formed β-sheets could also allow the binding of other unstructured monomers and small oligomers which could subsequently

undergo conformational conversions into β-sheets (*e.g.*, ~85, 200 ns in Fig. 2a) – also known as the secondary nucleation process[56, 57]. These newly nucleated small β-sheets could diffuse with respect to each other along their surfaces and merge into a larger single β-sheet nanostructure (Fig. 2a). Independently nucleated β-sheets could also coagulate with each other (e.g., ~80 ns in Fig. 2b, and ~125 ns in Fig. 2c) and re-arrange themselves (e.g, ~139 to 200 ns in Fig. 2b) into either two- (~139, 200, and 295 ns in Fig. 2b) or three-layered (~190ns in Fig. 2c) large β-sheet aggregates. Overall, the self-assembly dynamics of A1H1 into well-ordered β-sheet nanostructures is a complex multistep process, which involves the primary and secondary nucleation of β-sheet aggregates and the aggregation growth via elongation and coagulation. The oligomerization and fibrillization dynamics of A1H1 at the molecular and atomic levels might offer molecular insights to the amyloidogenesis in general.

To further characterizer the A1H1 self-assembly process, we computed the potential of mean force (PMF, i.e., the effective aggregation free energy landscape) as a function of the oligomer size ($n_{oligomer}$) and the average number of residues adopting β-sheet conformations per peptide ($n_{β-sheet}$) (Fig. 2d&e). All the 350 ns DMD trajectories from independent simulations at temperatures around ~0.51 were included in the analysis to capture the early assembly process. There were two well-defined energy basins around (1, 0) and (20, 8), corresponding to the isolated monomers and the ordered β-sheet-rich nano-assemblies, respectively. A saddle point located around ($n_{oligomer}$ = 4, $n_{β-sheet}$ =2) suggested that the critical nucleation size[46, 48, 50, 62] for A1H1 aggregation was approximately 4. When the oligomers size was less than 4, the lowest energy basin had $n_{β-sheet}$ ~ 0 indicating that these small oligomers predominantly adopted non β-sheet structures. As the oligomer size was larger than 4, the lowest free energy state had $n_{β-sheet}$ ~6-9 out of 12 total residues per chain, consistent with the formation of β-sheet rich fibril-like structures. The deep minimum around basin (20,8) indicated a high propensity of A1H1 to form multi-layered β-sheet as observed in prior experiments[35, 42].

The structure stability of A1H1 assemblies displayed thermo- and pH-dependence. The assemblies of suckerin family proteins are temperature- and pH-dependent, enabling novel applications in 3D printing, biomedicine, and bio-nanotechnology[4, 37, 39, 40]. For instance, the thermos-plasticity allowed suckerin assemblies to be melted and reshaped multiple times without the loss of mechanical properties[4, 37, 39, 40, 63]. The pH-dependent self-assembly formation could be used to encapsulate hydrophobic drugs for controlled release under the acidic environment. The histidine-containing M1 motifs with the ability to form β-rich aggregates are believed to play a key role in the pH- and temperature-responsive properties of suckerin assemblies[33, 38]. Therefore, we systematically tested the structural stability of A1H1 assemblies at 16 different temperatures ranging from 0.50 to 0.65 in neutral and acidic (all histidine residues protonated) solution environments. In addition to the most probable double-layer β-sheet nanostructures selected from DMD simulations at T~0.50-0.52, we also reconstructed two ideal fibril structures assuming parallel or anti-parallel alignment of β-strands (Fig. 3a). The reconstructed fibril structures were optimized with 50 ns DMD simulations at a low temperature T=0.50 (Fig. S1b&c), after which β-sheets of both structures adopted a left-handed twist consistent with many experimental observation of left-handed amyloid fibrils[26, 64-66 67]. Especially, the ideal parallel fibril (type B) after 50 ns simulations

featured the inter β-sheet distance of ~5.7 Å near the alanine-rich terminal and ~7.7 Å near the histidine-rich terminal, consistent with the computational results in Ref.[35] where similar fibrils were constructed according to X-ray scattering experiments. Since acetonitrile was added to promote the aggregation of A1H1 in water experimentally[35, 42], it was possible that the polar aprotic co-solvent was driving the formation of the densely packed parallel fibrils. Without acetonitrile co-solvents in our simulations, the self-assembled aggregates featured both parallel and anti-parallel β-sheets with defects and imperfect alignments (Fig. 1g) and thus higher potential energies than ideal parallel fibrils (Fig. S1). For each type of nano-fibrils at a given temperature, ten independent unbiased 250-ns DMD simulations with randomized initial velocities were performed to ensure sufficient sampling.

Using the last 50 ns of all independent simulations, the average secondary structure contents was calculated as the function of temperature for each type of fibrils (Fig. 3b&c). The β-sheet content in all the three types of fibrils featured a sigmoidal-like melting cure. The β-sheet melting temperature of self-assembled fibrils was around $T_m \sim 0.57$, which was higher than the corresponding aggregation transition temperature $T_{agg} \sim 0.55$. The melting temperatures of parallel ($T_m \sim 0.59$) and anti-parallel ($T_m \sim 0.58$) fibrils were slightly higher than that of the self-assembled ones because of lower potential energies with more ordered initial conformations. Under the acidic environment, the stability of pre-formed fibrils was reduced (Fig. 3c) with melting temperatures significantly lower than the corresponding values in the neutral solution environment (Fig. 3b). In the case of self-assembled fibrils, the β-sheet content at low pH started to decrease even at low temperatures ~0.50-0.52. The observed destabilization of fibrils was determined by the electrostatic repulsion between the protonated histidine residues at low pH.

Similar to the self-assembly simulations (Fig. 1d-f), structural analysis of various species during the last 50 ns of dissociation simulations was performed at each temperature for different types of fibrils in neutral and acidic environments (Fig. 4a,b). The size distribution changes of oligomers, β-sheet oligomers, and β-sheets with increasing temperatures coincided with the changes of β-sheet contents upon melting (Fig. 3), indicating that the loss of β-sheets in A1H1 assemblies was accompanied by their dissociation into monomers. For instance, self-assembled fibrils in the neural environment stayed intact with increasing temperatures until T ~ 0.55-0.56 (Fig. 4a,c and a typical trajectory at T=0.60 in Fig. S2a). As the temperature increasing up to 0.58, the fibrils started to dissociate into smaller oligomers with shorter β-sheets (Fig. 4a,c and T=0.58 in Fig. S2a). No stable oligomers and β-sheets were observed at temperatures higher than 0.60 (Fig. 4a,c and T=0.60 in Fig. S2a). However, under the acidic condition, even at the lowest temperature of 0.50 the self-assembled fibril dissociated into smaller β-sheet oligomers with sizes much less than the initial size of 20 (Fig. 4b,d and T=0.50 in Fig. S2b). As the temperature increased to 0.53, the β-sheet structures began to break into unstructured monomers (Fig 4d). At T=0.55, unstructured monomers became the most populated species. The ideal fibrils displayed a similar thermo- and pH-dependent dissociation as the self-assembled fibrils, but with higher melting temperatures (Fig. S3~S6).

Thermal hysteresis and pH-dependence of A1H1 assemblies. Our analyses of the association and dissociation dynamics of A1H1 self-assembly at difference temperatures

demonstrated a thermal hysteresis of the aggregates - i.e., the melting temperature of pre-formed A1H1 β-sheet assemblies was higher than the aggregation transition temperature from isolated monomers (Fig. 5a). The phenomenon is characteristic to first-order phase transitions with high energy barriers. As depicted in Fig. 5b, the isolated unstructured monomers corresponded to the high entropy and high energy state, while the highly ordered β-sheet aggregates with well-defined structures represented the low entropy and low energy state (e.g., the two deep basins in the aggregation free energy landscape of Fig. 2d,e). Due to the competition between enthalpy and entropy, the system underwent the phase transition at the aggregation transition temperature from the disordered monomeric state to the ordered fibril-like state. Each peptide in the β-sheet aggregates was stabilized by a network of backbone hydrogen bonds and side-chain packing, constituting a high energy barrier for the dissociation of pre-formed aggregates, $\Delta G^{\neq}$. At the aggregation transition temperature, the timescale required crossing the high enthalpy barrier, $\tau \sim \exp(\Delta G^{\neq}/k_B T)$, was likely longer than the simulation timescale and thus the dissociation of the fibril was not observed during the course all of our independent simulations. Only at higher temperatures with reduced dissociation times to cross the energy barrier, the dissociation was observed. Under the acidic environment, electrostatic repulsion between the protonated histidines reduced the energy barrier, resulting into a lower melting temperature. The thermal hysteresis of A1H1 β-rich assemblies allowed a wide temperature range for the ordered aggregation structures to maintain their mechanical properties, while the reduced structural stability in the acidic environment enabled the application of pH-dependent release of encapsulated drugs.

Conclusion

We systematically studied the self-assembly and dissociation dynamics of A1H1 peptides at different temperatures in both the neutral and acidic solution environments by performing all-atom DMD simulations. Our simulation results showed that twenty A1H1 peptides could readily aggregate into β-sheet rich nanostructures below a critical aggregation transition temperature T_{agg} under the neutral solution environment. The self-assembly dynamics of A1H1 from isolated unstructured monomers to well-defined β-sheet nanostructures was a complex multistep process, which involved both primary and secondary nucleation of β-sheets and the aggregation growth of β-sheets via elongation and coagulation. The aggregation free energy landscape analysis suggested that the critical nucleus size of A1H1 aggregation was around 4. The melting temperature T_m of pre-formed A1H1 β-sheet nanostructures was significantly higher than T_{agg} under the same solution condition. The observed thermal hysteresis of A1H1 assemblies was characteristic to first-order phase transitions with high energy barriers. In the acidic environment where all histidine residues were protonated, the stability of β-sheet nanostructures was significantly reduced and the highly ordered A1H1 β-sheet aggregates were easily disrupted at temperatures lower than T_{agg} into isolated monomers adopting coil conformations. Overall, our DMD simulations provided molecular insights to the thermo- and pH-dependence of A1H1 assemblies[35] and uncovered their self-assembly process at the atomic and molecular level.

With sequences comprised of repeating units of M1 and M2 motifs, suckerin family proteins resemble block copolymers and their self-assemblies also featured the thermo- and

pH-responsive properties as those stimuli-responsive smart materials by the synthesis of block copolymers[1-3]. Owing to the advantages of high designability in the sequence space, monodispersed synthesis, excellent biocompatibility and low immunogenicity, the peptide-based stimuli-responsive smart materials are expected to have broad applications in biomedicine, such as tissue regeneration, drug delivery and release, and 3D printed medical devices. Given the vast sequence space of peptides, an accurate modeling of the corresponding assembly structures and dynamics will be very useful in the design of peptide-based stimuli-responsive smart materials tailored for specific applications. By recapitulating the experimentally observed pH- and temperature-responses of A1H1 peptide assemblies, our computational results not only offered molecular insights for better understanding the supramolecular assembly structures and functions of the large suckerin family, but also provided a predictive computational tool for the future design of smart stimuli-responsive materials using peptides.

Materials and Methods

Molecular systems. The sequence of A1H1 peptide used in our simulation is AATAVSHTTHHA, commonly found in suckerin family proteins[35, 42, 43]. Since the A1H1 fragments are flanked by prolines and glycine-rich M2 modules without charged residues in full-length sukerin proteins, both N- and C-termini were treated neutral both in neutral and acidic environments. With increasing computational costs required for larger molecular systems to reach equilibrium, we chose a system size of 20 A1H1 peptides based on previous computational aggregation studies of other short amyloid peptides suggesting that 20 peptides could readily form stable cross-β aggregates[46, 48, 50]. The periodic boundary condition was used to mitigate the finite-size effect, known to determine the temperature ranges for co-existing phases but not the transition temperatures in first-order phase transitions, such as amyloid aggregation. We studied the aggregation of A1H1 at temperatures ranging from 0.50 to 0.60 in the reduced DMD temperature unit, kcal/(mol·k_B) ~500 K, where k_B is the Boltzmann constant. For each temperature, we performed 20 independent 350-ns DMD simulations starting from different initial coordinates and velocities. The initial configurations were constructed with fully-stretched A1H1 peptides randomly oriented and positioned in a cubic simulation box with a dimension of ~13.1 nm, chosen to be large enough to fit 20 peptides with the minimum inter-molecular distance of 1.5 nm but also small enough to have relatively high peptide centration for efficient observation of self-association and fibrillization *in silico*[68]. The corresponding peptide concentration was ~14.78 mM. At each temperature, an accumulative 7.0 μs simulations were performed. Replica exchange DMD simulations[69] were also performed for the same molecular system. However, with large energy gaps between the aggregated and non-aggregated states of the 20-peptide system, replicas were always divided into low and high temperature groups between which no successful exchanges were observed (data not shown). Interestingly, the temperature range without successful exchanges was consistent with the aggregation transition temperature observed from constant temperature simulations. However, with the lack of exchanges between all neighboring replicas required for accurate thermodynamics analyses, we chose the constant temperature simulations for our current study.

Three types of A1H1 β-sheet nanostructure (type A, B and C in Fig. 3a) were used in the dissociation simulations under the neutral or acidic environments. In the acidic condition, all the histidine was protonated with a net charge of +1e assuming the pH was lower than the isoelectric pH of ~6.0. The type A fibril (shown in Fig. 3a and S1a) with both parallel and anti-parallel alignments of β-strands were obtained self-assembly simulations at low temperatures 0.50-0.52. Ideal parallel (type B fibril, shown in Fig. 3a and S1b) and anti-parallel (type C fibril, shown in Fig. 3a and S1c) fibrils were built using our in-house code and optimized with 50-ns DMD simulations at a low temperature of 0.50 (Fig. S1b&c). The dissociation simulations of A1H1 assemblies were performed at temperatures ranging from 0.50 to 0.65 in both neutral and acidic environment conditions. For each type of fibrils, ten independent 250-ns DMD simulations were performed with the accumulative simulations time of ~2.5 μs at each of the temperatures and solution conditions. The size of the simulation box was the same as the self-assembly simulation used.

Discrete molecular dynamics Simulations. All simulations were performed in the canonical NVT ensemble using the all-atom discrete molecular dynamics (DMD)[69, 70] simulations. DMD is a unique type of molecular dynamics algorithm[44], where the continuous potential functions in the traditional MD simulations were modeled by discrete step functions. With significantly enhanced sampling efficiency, DMD simulations were widely used by various groups in studying protein folding[71], amyloid aggregation[46, 72, 73], and nanoparticle-protein interactions[51, 64, 74]. The force field used in our DMD simulation was adopted from the traditional MD simulations that have been discussed in our previous studies[48, 61]. Both bonded interactions (covalent bonds, bond angles, and dihedrals) and non-bonded interactions (van der Waals, solvation, hydrogen bond, and electrostatic terms) were included. The units of mass, time, length, and energy in this simulation were 1 g/mol, 50 fs, 1 Å, and 1 kcal/mol, respectively. The temperature was maintained by the Anderson thermostat. We assigned a mean thermal collision time of 0.5 ps for each atom, chosen to be significantly longer than typical autocorrelation times of atoms in macromolecules and thus minimally perturb the dynamic proprieties[75].

Analysis methods. The secondary structures were determined using the dictionary secondary structure of protein (DSSP) method[76]. A hydrogen bond was defined if the distance between backbone N and O atoms was ≤3.5 Å and the angle of N−H···O ≥120°[50]. Two peptides were considered to form a β-sheet, if at least two consecutive residues in each chain adopted the β-strand conformation and the two peptides had at least two backbone hydrogen bonds[46, 48, 52]. The anti-parallel/parallel β-strand ratio was determined by comparing the number of hydrogen bonds between any two adjacent β-strands forming anti-parallel or parallel β-sheets[48]. The size of a β-sheet was denoted as the number of strands in a β-sheet layer. As in our previous studies[46, 50], the average β-sheet size was weighted according to the size of each β-sheet.

A cutoff distance of 0.55 nm was used to define an atomic contact between heavy atoms (backbone or sidechain) of two non-consecutive residues along the sequence. If two peptides connected by at least one inter-molecule heavy atom contact, they belonged to the same oligomer. The number of peptides in an oligomer was referred as the oligomer size. A β-sheet oligomer was defined as multiple β-sheets inter-connected by at least one heavy atom contact,

and the total number of peptides in β-sheet conformation within the complex corresponded to the β-sheet oligomer size.

The potential of mean force (PMF, or the effective free energy) was computed according to $-k_BT ln P(n_{oligomer\ size}, n_{\beta\text{-}sheet\ residue})$, where T was the simulation temperature and $P(n_{oligomer\ size}, n_{\beta\text{-}sheet\ residue})$ was the probability of finding an oligomer with the oligomer size $n_{oligomer\ size}$ and the average number of residues adopting β-sheet conformation per chain, $n_{\beta\text{-}sheet\ residue}$.

Supporting Information
Supplementary Figures S1-S6 (PDF)

Author Information
Corresponding authors
*E-mail: sunyunxiang@nbu.edu.cn, fding@clemson.edu

Acknowledgement

References

1.   M. A. Stuart, W. T. Huck, J. Genzer, M. Muller, C. Ober, M. Stamm, G. B. Sukhorukov, I. Szleifer, V. V. Tsukruk, M. Urban, F. Winnik, S. Zauscher, I. Luzinov and S. Minko, *Nature materials*, 2010, **9**, 101-113.

2.   X. Yan, F. Wang, B. Zheng and F. Huang, *Chem Soc Rev*, 2012, **41**, 6042-6065.

3.   J. M. Zhuang, M. R. Gordon, J. Ventura, L. Y. Li and S. Thayumanavan, *Chem Soc Rev*, 2013, **42**, 7421-7435.

4.   P. A. Guerette, S. Hoon, Y. Seow, M. Raida, A. Masic, F. T. Wong, V. H. B. Ho, K. W. Kong, M. C. Demirel, A. Pena-Francesch, S. Amini, G. Z. Tay, D. Ding and A. Miserez, *Nat Biotechnol*, 2013, **31**, 908-915.

5.   G. Askarieh, M. Hedhammar, K. Nordling, A. Saenz, C. Casals, A. Rising, J. Johansson and S. D. Knight, *Nature*, 2010, **465**, 236-238.

6.   F. Albericio, M. Alvarez, C. Cuevas, F. Andres, Y. Garcia-Ramos, P. Ruiz-Sanchis, S. Savina and J. Tulla-Puche, *J Pept Sci*, 2010, **16**, 23-23.

7.   J. Wang, K. Liu, R. R. Xing and X. H. Yan, *Chem Soc Rev*, 2016, **45**, 5589-5604.

8.   B. O. Okesola and A. Mata, *Chem Soc Rev*, 2018, **47**, 3721-3736.

9.   C. Guo, Y. Luo, R. H. Zhou and G. H. Wei, *Acs Nano*, 2012, **6**, 3907-3918.

10.   G. M. Whitesides and B. Grzybowski, *Science*, 2002, **295**, 2418-2421.

11.   P. W. Frederix, G. G. Scott, Y. M. Abul-Haija, D. Kalafatovic, C. G. Pappas, N. Javid, N. T. Hunt, R. V. Ulijn and T. Tuttle, *Nature chemistry*, 2015, **7**, 30-37.

12.   C. Guo, Z. A. Amon, R. X. Qi, Q. W. Zhang, L. Adler-Abramovich, E. Gazit and G. H. Wei, *Acs Nano*, 2016, **10**, 8316-8324.

13.   R. V. Ulijn and A. M. Smith, *Chem Soc Rev*, 2008, **37**, 664-675.

14.   M. R. Ghadiri, J. R. Granja, R. A. Milligan, D. E. Mcree and N. Khazanovich, *Nature*, 1993, **366**, 324-327.

15.   M. Reches and E. Gazit, *Nano Lett*, 2004, **4**, 581-585.

16.   H. Xu, J. Wang, S. Y. Han, J. Q. Wang, D. Y. Yu, H. Y. Zhang, D. H. Xia, X. B. Zhao, T. A. Waigh and J. R. Lu, *Langmuir*, 2009, **25**, 4115-4123.

17.   A. Undas and R. A. S. Ariens, *Arterioscl Throm Vas*, 2011, **31**, E88-E99.

18.   I. Delon and N. H. Brown, *Curr Opin Cell Biol*, 2007, **19**, 43-50.

19.   P. A. Guerette, S. Hoon, D. W. Ding, S. Amini, A. Masic, V. Ravi, B. Venkatesh, J. C. Weaver and A. Miserez, *Acs Nano*, 2014, **8**, 7170-7179.

20.   M. S. Dueholm, M. Albertsen, D. Otzen and P. H. Nielsen, *Plos One*, 2012, **7**, e51274.

21.   M. S. Dueholm, M. T. Sondergaard, M. Nilsson, G. Christiansen, A. Stensballe, M. T.

Overgaard, M. Givskov, T. Tolker-Nielsen, D. E. Otzen and P. H. Nielsen, *Microbiologyopen*, 2013, **2**, 365-382.

22.   G. Nystrom, M. P. Fernandez-Ronco, S. Bolisetty, M. Mazzotti and R. Mezzenga, *Adv Mater*, 2016, **28**, 472-478.

23.   S. Bolisetty and R. Mezzenga, *Nat Nanotechnol*, 2016, **11**, 365-371.

24.   D. R. Booth, M. Sunde, V. Bellotti, C. V. Robinson, W. L. Hutchinson, P. E. Fraser, P. N. Hawkins, C. M. Dobson, S. E. Radford, C. C. F. Blake and M. B. Pepys, *Nature*, 1997, **385**, 787-793.

25.   Y. Miller, B. Ma and R. Nussinov, *Chem Rev*, 2010, **110**, 4820-4838.

26.   P. C. Ke, M. A. Sani, F. Ding, A. Kakinen, I. Javed, F. Separovic, T. P. Davis and R. Mezzenga, *Chem Soc Rev*, 2017, **46**, 6492-6531.

27.   M. Baram, Y. Atsmon-Raz, B. Y. Ma, R. Nussinov and Y. Miller, *Physical Chemistry Chemical Physics*, 2016, **18**, 2330-2338.

28.   B. Wang, E. H. Pilkington, Y. Sun, T. P. Davis, P. C. Ke and F. Ding, *Environmental science. Nano*, 2017, **4**, 1772-1783.

29.   P. C. Ke, E. H. Pilkington, Y. Sun, I. Javed, A. Kakinen, G. Peng, F. Ding and T. P. Davis, *Adv Mater*, 2019, DOI: 10.1002/adma.201901690, e1901690.

30.   T. P. Knowles, M. Vendruscolo and C. M. Dobson, *Nature reviews. Molecular cell biology*, 2014, **15**, 384-396.

31.   T. P. J. Knowles and M. J. Buehler, *Nat Nanotechnol*, 2011, **6**, 469-479.

32.   D. M. Fowler, A. V. Koulov, W. E. Balch and J. W. Kelly, *Trends Biochem Sci*, 2007, **32**, 217-224.

33.   D. W. Ding, J. Pan, S. H. Lim, S. Amini, L. F. Kang and A. Miserez, *J Mater Chem B*, 2017, **5**, 8467-8478.

34.   D. W. Ding, P. A. Guerette, J. Fu, L. H. Zhang, S. A. Irvine and A. Miserez, *Adv Mater*, 2015, **27**, 3953-3961.

35.   S. H. Hiew, A. Sanchez-Ferrer, S. Amini, F. Zhou, J. Adamcik, P. Guerette, H. B. Su, R. Mezzenga and A. Miserez, *Biomacromolecules*, 2017, **18**, 4240-4248.

36.   D. W. Ding, P. A. Guerette, S. Hoon, K. W. Kone, T. Cornvik, M. Nilsson, A. Kumar, J. Lescar and A. Miserez, *Biomacromolecules*, 2014, **15**, 3278-3289.

37.   S. H. Hiew and A. Miserez, *Acs Biomater Sci Eng*, 2017, **3**, 680-693.

38.   Y. Ping, D. Ding, R. Ramos, H. Mohanram, K. Deepankumar, J. Gao, G. Tang and A. Miserez, *Acs Nano*, 2017, **11**, 4528-4541.

39.   C. Rieu, L. Bertinetti, R. Schuetz, C. C. A. Salinas-Zavala, J. C. Weaver, P. Fratzl, A. Miserez and A. Masic, *Bioinspir Biomim*, 2016, **11**, 055003.

40.   V. Latza, P. A. Guerette, D. W. Ding, S. Amini, A. Kumar, I. Schmidt, S. Keating, N. Oxman, J. C. Weaver, P. Fratzl, A. Miserez and A. Masic, *Nat Commun*, 2015, **6**, 8313.

41.   A. Kumar, H. Mohanram, K. W. Kong, R. Goh, S. Hoon, J. Lescar and A. Miserez, *Biomater Sci-Uk*, 2018, **6**, 2440-2447.

42.   A. Sanchez-Ferrer, J. Adamcik, S. Handschin, S. H. Hiew, A. Miserez and R. Mezzenga, *Acs Nano*, 2018, **12**, 9152-9161.

43.   S. H. Hiew, P. A. Guerette, O. J. Zvarec, M. Phillips, F. Zhou, H. B. Su, K. Pervushin, B. P. Orner and A. Miserez, *Acta Biomater*, 2016, **46**, 41-54.

44.   D. Shirvanyants, F. Ding, D. Tsao, S. Ramachandran and N. V. Dokholyan, *The journal of*

physical chemistry. B, 2012, **116**, 8375-8382.

45. B. Urbanc, M. Betnel, L. Cruz, G. Bitan and D. B. Teplow, *J Am Chem Soc*, 2010, **132**, 4266-4280.

46. Y. Sun, A. Kakinen, Y. Xing, P. Faridi, A. Nandakumar, A. W. Purcell, T. P. Davis, P. C. Ke and F. Ding, *Small*, 2019, **15**, e1805166.

47. S. Peng, F. Ding, B. Urbanc, S. V. Buldyrev, L. Cruz, H. E. Stanley and N. V. Dokholyan, *Phys Rev E*, 2004, **69**.

48. Y. X. Sun, X. W. Ge, Y. T. Xing, B. Wang and F. Ding, *Sci Rep-Uk*, 2018, **8**, 10353.

49. X. Ge, Y. Sun and F. Ding, *Biochimica et biophysica acta. Biomembranes*, 2018, **1860**, 1687-1697.

50. Y. Sun, B. Wang, X. Ge and F. Ding, *Physical chemistry chemical physics : PCCP*, 2017, **19**, 28414-28423.

51. Y. X. Sun, A. Kakinen, C. Zhang, Y. Yang, A. Faridi, T. P. Davis, W. G. Cao, P. C. Ke and F. Ding, *Nanoscale*, 2019, **11**, 11933-11945.

52. Y. X. Sun, Z. Y. Qian, C. Guo and G. H. Wei, *Biomacromolecules*, 2015, **16**, 2940-2949.

53. K. Eden, R. Morris, J. Gillam, C. E. MacPhee and R. J. Allen, *Biophys J*, 2015, **108**, 632-643.

54. P. Arosio, T. P. J. Knowles and S. Linse, *Physical Chemistry Chemical Physics*, 2015, **17**, 7606-7618.

55. C. Galvagnion, A. K. Buell, G. Meisl, T. C. T. Michaels, M. Vendruscolo, T. P. J. Knowles and C. M. Dobson, *Nat Chem Biol*, 2015, **11**, 229.

56. R. Gaspar, G. Meisl, A. K. Buell, L. Young, C. F. Kaminski, T. P. J. Knowles, E. Sparr and S. Linse, *Quarterly reviews of biophysics*, 2017, **50**, e6.

57.   S. Linse, *Biophysical reviews*, 2017, **9**, 329-338.

58.   A. Villar-Pique, A. Espargaro, S. Ventura and R. Sabate, *Biotechnol J*, 2016, **11**, 172-177.

59.   N. Benseny-Cases, M. Cocera and J. Cladera, *Biochem Bioph Res Co*, 2007, **361**, 916-921.

60.   G. Reddy, J. E. Straubb and D. Thirumalai, *P Natl Acad Sci USA*, 2009, **106**, 11948-11953.

61.   Y. Sun, A. Kakinen, Y. Xing, E. H. Pilkington, T. P. Davis, P. C. Ke and F. Ding, *Biochimica et biophysica acta. Molecular basis of disease*, 2019, **1865**, 434-444.

62.   Y. Zou, Y. X. Sun, Y. Z. Zhu, B. Y. Ma, R. Nussinov and Q. W. Zhang, *Acs Chem Neurosci*, 2016, **7**, 286-296.

63.   A. Miserez, J. C. Weaver, P. B. Pedersen, T. Schneeberk, R. T. Hanlon, D. Kisailus and H. Birkedal, *Adv Mater*, 2009, **21**, 401-406.

64.   A. Faridi, Y. Sun, Y. Okazaki, G. Peng, J. Gao, A. Kakinen, P. Faridi, M. Zhao, I. Javed, A. W. Purcell, T. P. Davis, S. Lin, R. Oda, F. Ding and P. C. Ke, *Small*, 2018, **14**, e1802825.

65.   Y. Li, C. Zhao, F. Luo, Z. Liu, X. Gui, Z. Luo, X. Zhang, D. Li, C. Liu and X. Li, *Cell research*, 2018, **28**, 897-903.

66.   A. Kakinen, Y. Sun, I. Javed, A. Faridi, E. H. Pilkington, P. Faridi, A. W. Purcell, R. Zhou, F. Ding, S. Lin, P. Chun Ke and T. P. Davis, *Science bulletin*, 2019, **64**, 26-35.

67.   G. Nystrom, M. Arcari and R. Mezzenga, *Nat Nanotechnol*, 2018, **13**, 330-336.

68.   D. Matthes, V. Gapsys and B. L. de Groot, *Journal of molecular biology*, 2012, **421**, 390-416.

69.   F. Ding, D. Tsao, H. Nie and N. V. Dokholyan, *Structure*, 2008, **16**, 1010-1018.

70.   N. V. Dokholyan, S. V. Buldyrev, H. E. Stanley and E. I. Shakhnovich, *Folding & design*, 1998, **3**, 577-587.

71.   N. I. Brodie, K. I. Popov, E. V. Petrotchenko, N. V. Dokholyan and C. H. Borchers, *Sci Adv*,

2017, **3**, e1700479.

72.   Y. M. Wang, S. J. Bunce, S. E. Radford, A. J. Wilson, S. Auer and C. K. Hall, *P Natl Acad Sci USA*, 2019, **116**, 2091-2096.

73.   B. Urbanc, M. Betnel, L. Cruz, H. Li, E. A. Fradinger, B. H. Monien and G. Bitan, *Journal of molecular biology*, 2011, **410**, 316-328.

74.   M. Wang, Y. Sun, X. Cao, G. Peng, I. Javed, A. Kakinen, T. P. Davis, S. Lin, J. Liu, F. Ding and P. C. Ke, *Nanoscale*, 2018, **10**, 19995-20006.

75.   H. Tanaka, K. Nakanishi, and N. Watanabe, *J. Chem. Phys.*, 1983, **78**, 2626-2634.

76.   W. Kabsch and C. Sander, *Biopolymers*, 1983, **22**, 2577-2637.

Figure Captions

Figure 1. **Conformational analysis of self-assembled A1H1 aggregates**. a) The average secondary structure contents for unstructured (including random coil and bend) conformation, β-sheets, turns and helixes at different temperatures. b) The average number of hydrogen bonds in β-sheet (colored in purple) and non-β-sheet (colored in black) structures. c) The percentages of hydrogen bonds in non-β-sheet conformation (colored in black), anti-parallel (cyan) and parallel (purple) alignment of neighboring β-strands. The size distribution of oligomers (d) and β-sheet oligomers (e), the mass-weighted average β-sheet size (f) at different temperatures. (g) The residue-wise contact frequency maps based on backbone and sidechain atoms at low temperatures 0.50-0.52, where the β-rich aggregates were observed in simulations. Representative self-assemblies comprised of (h) one-, (i) two- and (j) three-layered β-sheets are also shown. For each temperature, the last 100 ns trajectories from 20 independent 350-ns DMD simulations were used for the analyses.
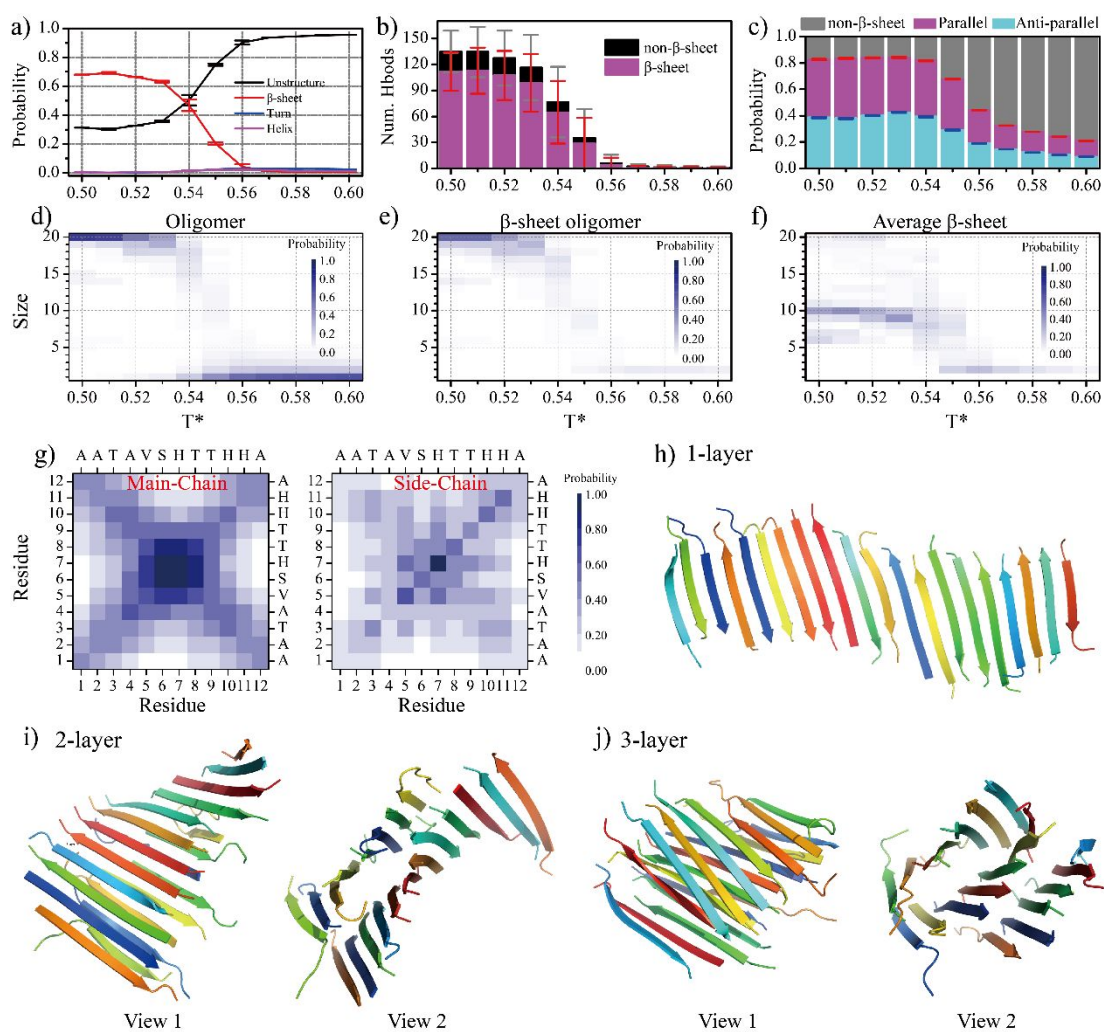
Figure 2. The self-assembly dynamics of twenty A1H1 peptides. Representative self-assembly trajectories from isolated monomers into final a) 1-layered, b) 2-layered and c) 3-layered β-sheet aggregates are selected to demonstrate the aggregation process. Sizes of the largest oligomer (blue), the largest β-sheet (red), and the largest β-sheet oligomer (purple) as well as the mass-weighted average β-sheet size (black) are plotted as a function of the simulation time. The self-assembly structures at times as indicated by blue arrows are also shown in the inset, where peptides are shown in the cartoon representation. The potential of mean force (PMF) as a function of the oligomer size ($n_{oligomer}$) and the average number of residues adopting β-sheet conformations per chain ($n_{\beta\text{-sheet residues}}$) are presented as d)

three-dimensional surface and e) two-dimensional contour plots. Representative snapshot oligomer structures are shown along the aggregation pathways from isolated monomers to the final β-sheet rich aggregates.
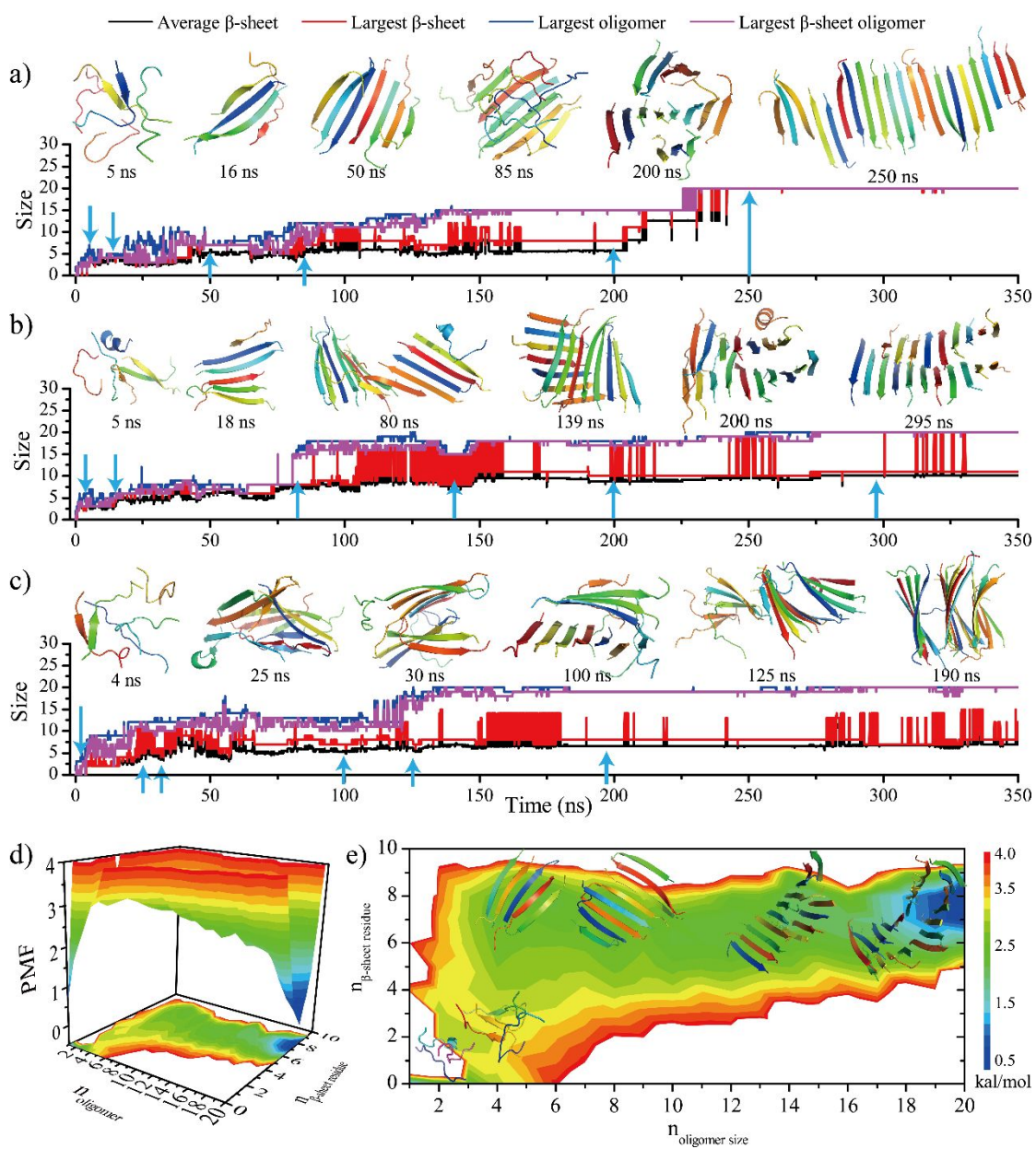
Figure 3. Secondary structure changes of pre-formed A1H1 β-sheet nano-fibrils at different temperatures in neutral and acidic environments. a) Three different types of A1H1 fibrils were used in dissociation simulations. Type-A fibril was obtained from assembly simulations at low temperature, where both parallel and anti-parallel β-sheets were observed. Ideal parallel (type B) and anti-parallel (type C) fibrils were also reconstructed and optimized with 50 ns low temperature simulations at T=0.50. For each type of nano-fibrils, the averaged secondary structure content changes in terms of the unstructured conformation, β-sheet, turn and helix are shown as the function of increasing temperatures in the b) neutral and c) acidic environments. For each temperature, 10 independent 250-ns simulations were performed and the last 50 ns trajectories were used in the analyses.

Figure 4. The dissociation dynamics of self-assembled nano-fibrils at different temperatures in neural and acidic environments. In a) neutral and b) acidic environments, the probability distributions of oligomer sizes, β-sheet oligomer sizes, and mass-weighted averaged β-sheet sizes are plotted at different temperatures for the dissociation simulations of the self-assembled nano-fibrils (type A in Fig. 3). The last 50 ns trajectories of the 10 independent 250-ns simulations were used. Representative dissociated structures of fibril A at low, near transition and high temperatures are selected from simulations in the c) neutral and d) acidic conditions.

Figure 5. The temperature- and pH-dependence of the A1H1 assemblies. a) The average β-sheet content as the function of temperature for the association simulations (black), the dissociation of self-assembled fibrils (type A) in neutral (red) and acid (blue) environments. b) The schematic diagram illustrates the thermal hysteresis of A1H1 self-assemblies, and also the enhanced dissociation at the acidic environment.
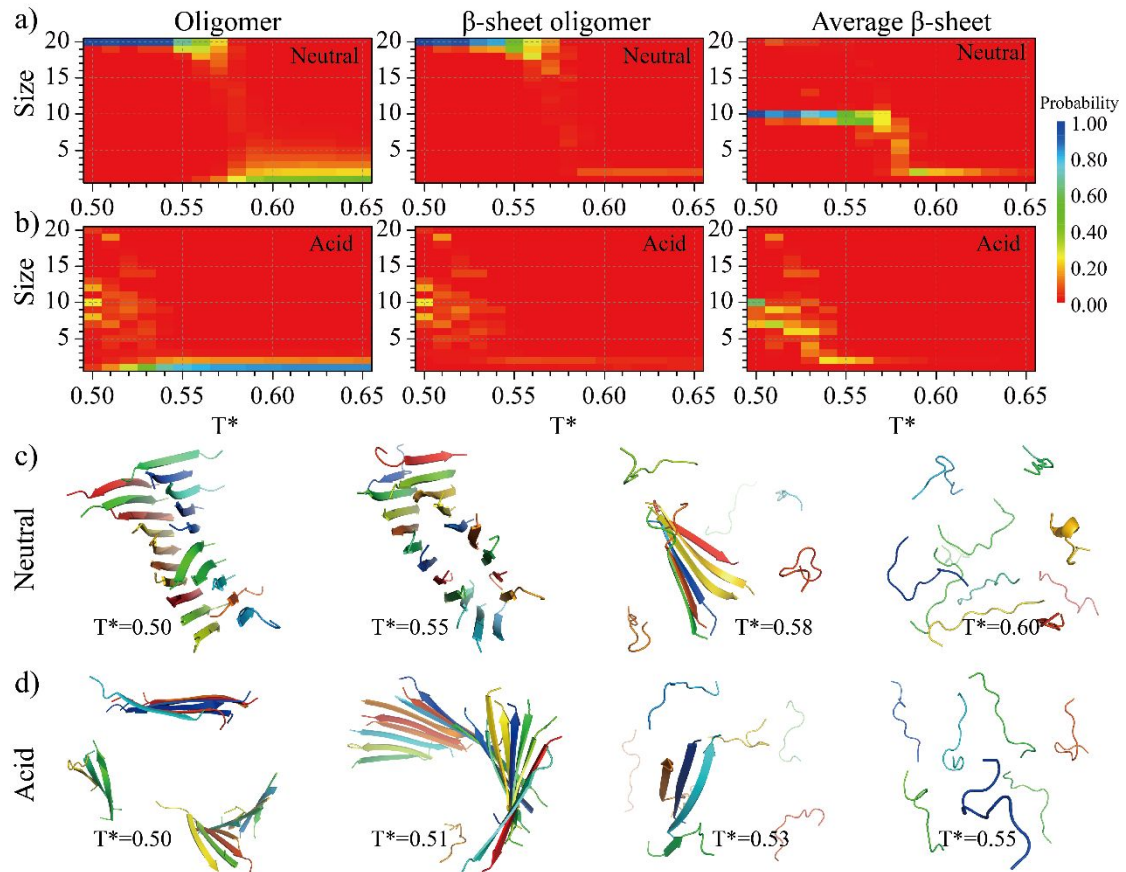
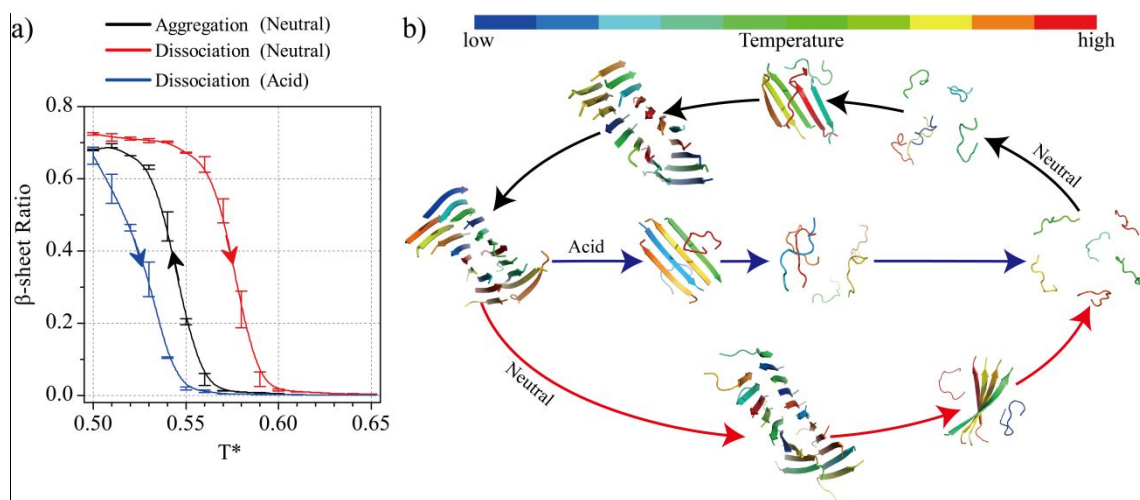**Figure 1**. **Conformational analysis of self-assembled A1H1 aggregates**.

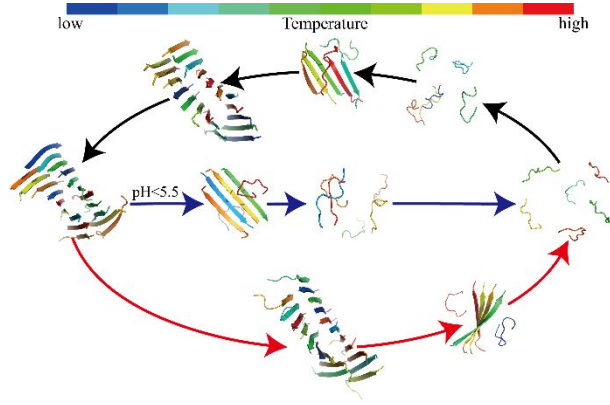**Figure 2. The self-assembly dynamics of twenty A1H1 peptides**.
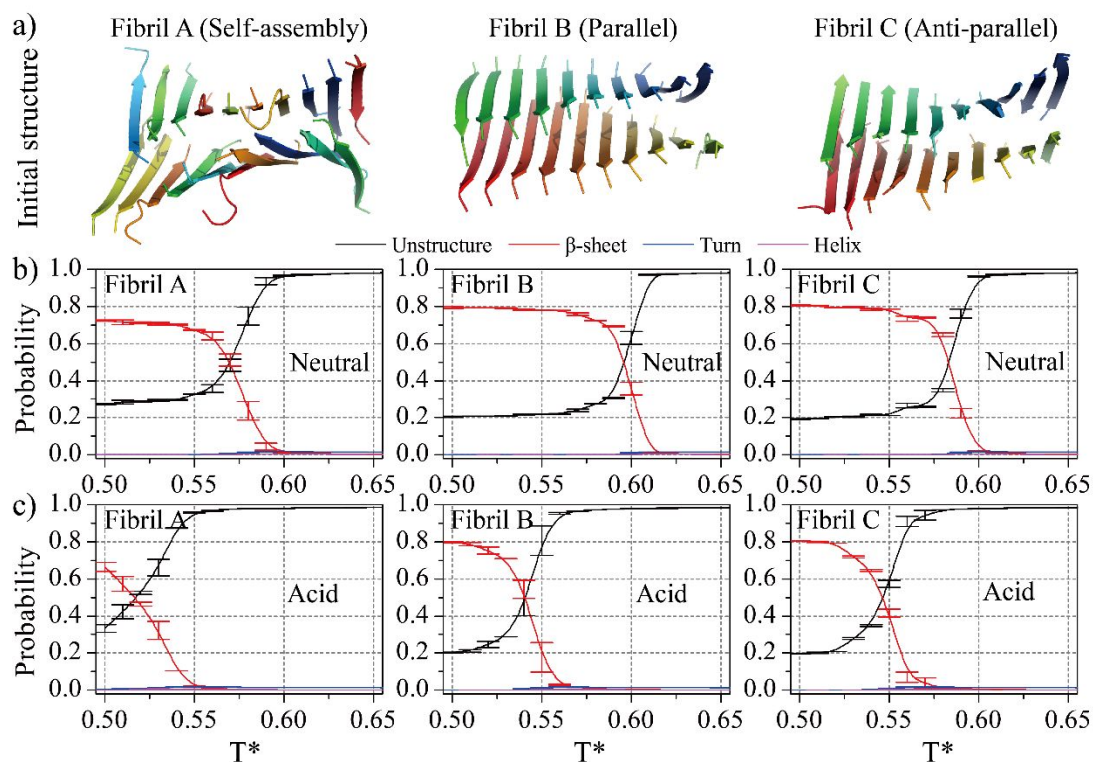
Figure 3. Secondary structure changes of pre-formed A1H1 β-sheet nano-fibrils at different temperature in neutral and acidic environments.

Figure 4. The dissociation dynamics of self-assembled nano-fibrils at different temperatures in neural and acidic environments.

Figure 5. The temperature- and pH-dependence of the A1H1 assemblies.

TOC